Faulty Feeder Detection for Single Phase-to-Ground Faults in Distribution Networks Based on Waveform Encoding and Waveform Segmentation

Jiawei Yuan, Zaibin Jiao, *Senior Member*, *IEEE*

***Abstract*— Faulty feeder detection helps ensure the stability and safety of power grids after single-phase-to-ground (SPG) faults occur in distribution networks. The existing detection techniques identify the faulty feeder by extracting representative fault features, while they fail to show reliable detection performance due to variable fault conditions and complex fault transients. To address these drawbacks, this paper proposes a method based on waveform encoding and waveform segmentation. Since the waveforms have complete fault features in fault signals, it is suitable to recognize the signals on the waveform scale, rather than extracting and fusing several fault features. Firstly, raw sampled zero-sequence voltage (ZSV) and zero-sequence current (ZSC) are processed by using the proposed encoding method, and the ZSV-ZSC image can be generated quickly. Secondly, to learn and understand the waveforms of ZSV and ZSC, a two-path fully convolutional network (FCN) is established to make pixel-wise prediction on the ZSV-ZSC image. Finally, the fault degree of each feeder can be estimated based on the segmented waveform in the ZSV-ZSC image. The performance evaluation is implemented in the NVIDIA Jetson Xavier embedded platform, and the experimental results demonstrate that the proposed method can identify the faulty feeder with high accuracy within 28 ms.**

***Index Terms*—Faulty-feeder detection, NVIDIA Jetson Xavier, waveform encoding, waveform segmentation, waveform understanding.**

I. Introduction

NON-EFFECTIVELY grounded networks are widely used in medium-voltage (MV) distribution networks due to the advantages of uninterrupted power supply [1-2]. During routine operation, the reliability of distribution networks is challenged by various faults, where the single-phase-to-ground (SPG) faults account for 80% of all faults [3]. After the occurrence of SPG faults, the fault currents are weak and the fault transients are complex, thus causing great difficulties for determining the specific faulty feeder. Serious faults and wide impacts, such as interphase short, fire hazards, and casualties, would occur if the faulty feeder cannot be accurately detected and timely isolated [4]. Therefore, to ensure the stability and safety of distribution networks, it is significant to propose an SPG faulty-feeder detection method with high detection accuracy and efficiency.

A. Previous and Related Work

In recent years, many detection techniques have been proposed, ranging from analysis-based methods [5-16] and learning-based methods [17-28]. For the analysis-based methods, it can be divided into steady-state methods [5-6] and transient methods [7-16]. The fault characteristics in the steady-state, such as amplitude, direction, power, and admittance, are utilized to construct the detection schemes, while the detection performance is easily affected by operating conditions, especially under the resonant grounding networks. Since the fault characteristics in the transient zero-sequence currents (TZSCs) are much larger than that in the stead-state currents (SSCs), the transient methods expect to extract rich fault features from TZSCs and identify the faulty feeder accordingly. The detection performance can be significantly improved if the transient features are effectively extracted. In [7], a fundamental component (FC) shift method is proposed to remove FC in the TZSCs, and transient features, such as transient energy, kurtosis, and cross-correlation distance, are extracted and fused by using multiple evidence estimation. In [8], the FC in the TZSCs can be removed by using fast Fourier transform (FFT) backstepping method, and both correlation characteristics in TZSCs and SSCs are combined to detect the faulty feeder. Furthermore, other popular signal processing algorithms are also applied in this field, such as wavelet transform (WT) [9]-[10], S-transform [11]-[12], empirical mode decomposition (EMD) [13]-[14], and variational mode decomposition (VMD) [15]-[16].

Inspired by the successful applications of artificial intelligence (AI) techniques, the learning-based methods are becoming increasing attractive for detection issues. The learning-based methods can further be classified into multi-feature fusion methods [17-24] and deep-learning methods [25-28]. For the multi-feature fusion methods, they usually extract several typical fault features to describe raw signals, and then the AI algorithms are used as tools for feature fusion. In [17], the frequency-spectrum energy and polarity characteristics are extracted by using WT, and they are fused for detection by using the ensemble learning algorithm. In [18], three intrinsic mode functions (IMFs), corresponding to the decaying direct current (DC) component, FC, and high-frequency component, are obtained through VMD, and they are learned by using long short-term memory neural network (LSTM). Furthermore, support vector machine [19]-[20], Bayesian techniques [21]-[22], and neural networks [23]-[24] are also used to combine the extracted fault features. Regarding the deep-learning methods, they can adaptively learn fault features from raw signals, instead of selecting several features based on experience, and then, classify the feeders based on the learned features, where the convolutional neural

This work was supported by the National Natural Science Foundation of China under Grant 52277124.

J. W. Yuan and Z. B. Jiao are with the School of Electrical Engineering, Xi'an Jiaotong University, Xi'an 710049, China (e-mail: yuanjiawei2019@163.com; jiaozaibin@mail.xjtu.edu.cn).

network (CNN) is usually applied. In [25], the CNN is used to learn and recognize the TZSC of each feeder, and its outputs directly correspond to the final identification results. In [26], the sampled data of TZSCs are added with each other to achieve the fused waveforms, and the CNN is applied to find the fused waveforms that do not contain the faulty feeder. In addition, CNNs with attention strategy [27] and transfer learning method [28] are also utilized to improve the discriminative capability.

B. Problems of Existing Detection Methods

1) The extracted features are insufficient. The existing analysis-based methods only extract several fault features from raw signals, where the selection of fault features is reliant on too many subjective factors, and they cannot ensure to cover all fault scenarios. Besides, the applied signal processing algorithms have inherent drawbacks: the existing FFT, WT, and S-transform utilize the fixed basis functions, resulting in poor feature representation ability [16]; EMD algorithm is prone to mode mixing and end effects [29]; the suitable number of decomposition layer by using VMD is difficult to determine, and the selection of IMFs heavily depends on experience. For the multi-feature fusion methods, they also have similar problems in the feature extraction process. Thus, the misjudgments of faulty feeder would inevitably occur when the extracted features fail.

2) The detection results lack credibility evaluation. Although the analysis-based methods can extract fault features with clear physical meaning, the constructed detection schemes usually adopt the voting method or different weights to combine the features, which is not always reliable. Moreover, the detailed detection process of learning-based methods is blind [30], especially for the deep-learning methods. That is, the learned high-level features lack clear physical meaning, which is difficult to verify its effectiveness, and the credibility of output results cannot be evaluated, resulting in unconvincing identification results of faulty feeder.

C. Contributions of the Proposed Method

This paper proposes a faulty feeder detection method based on the waveform encoding and waveform segmentation. Because the waveforms of raw signals have complete fault features, the signals are learned and understood from the perspective of waveform, thus avoiding information loss. The main contributions can be summarized as follows:

1) Instead of converting the numerical signals into images using the conventional plot method, this paper proposes a novel waveform encoding method, which can directly obtain the matrixes corresponding to the waveform images. Each element in the matrixes denotes a pixel in the images, and its value can be determined according to the amplitudes of sampling points over time. By using the proposed encoding method, the waveform images composed of zero-sequence voltage (ZSV) and zero-sequence current (ZSC) can be generated quickly, thus significantly improving the detection efficiency.

2) By making pixel-wise prediction using waveform segmentation method, all the pixels in the ZSV-ZSC images can be interpreted with clear meanings, and the complete waveforms can be identified, which are not limited to several fault features. To conduct waveform segmentation, a two-path fully convolutional network (FCN) is established, including the segmentation path and classification path. By the cooperation of two paths, the established FCN can have both detailed and overall understanding on the images, thereby greatly enhancing the segmentation accuracy.

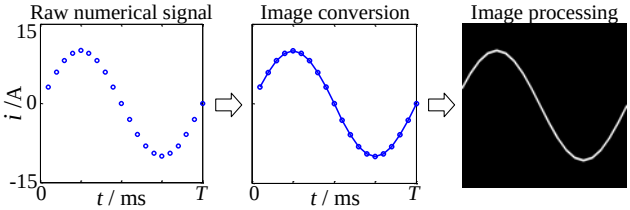

Fig. 1. Image creation by using 'plot' function.

3) Since the FCN can output the prediction on each pixel in the ZSV-ZSC images, the pixels with the same label can generate the segmented waveforms with specific meanings. Besides, the segmented waveforms can correspond to raw waveforms, and the credibility of recognition results can be easily evaluated by comparing the similarity between the segmented faulty-feeder ZSC and raw ZSC. Therefore, the interpretability in the detection process can be enhanced, and the credibility evaluation can guarantee the reliability of detection results.

4) The feasibility of the proposed method is implemented and verified in the embedded platform NVIDIA Jetson AGX Xavier. After the off-line training of the established two-path FCN, the detection performance is evaluated based on the online processor-in-the-loop (PIL) test. Moreover, large amounts of fault data are obtained from simulations, field test, and practical distribution networks. The experimental results show that the proposed method can achieve both good detection accuracy and high detection efficiency, demonstrating its considerable potential for future applications.

II. Waveform Encoding for Image Creation

For the fault signals identified by using deep convolutional neural networks (DCNN), it is necessary to convert the initial numerical data into images before recognition [31-32]. However, the image creation is quite time-consuming, while the protection schemes have high requirements for detection efficiency due to the reliability purpose. That is to say, the detection efficiency is one of the limiting factors for practical applications, especially for the learning-based methods. In fact, the electrical signals commonly satisfy sine functions owing to the rotation of the synchronous generator in power grids, which implies that the generated images have substantial sparsity.

For a sinusoidal signal, the protection devices obtain the sampled data by using the A/D conversion. Subsequently, the sampled data in numerical form can be converted into an image by using 'plot' function, which corresponds to connecting two adjacent sampling points with a straight line. The generated image would require further cropping and binary operations. Finally, the image for recognition can be obtained. The whole procedure for image creation is shown in Fig. 1.

Evidently, the sinusoidal waveform only accounts for a small part of the generated image, while most regions are colored in black. However, the image creation by using 'plot' function does not take the sparsity characteristic into consideration, thus resulting in huge computation cost. Especially, the image-recognition-based methods use the trained model for

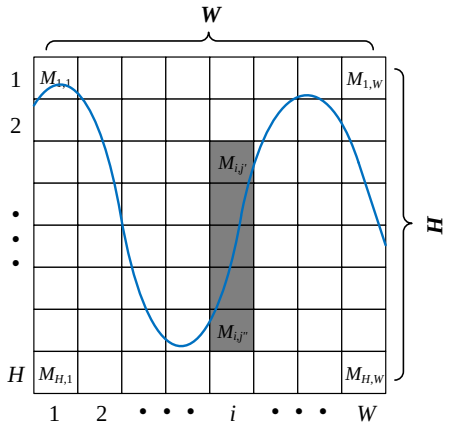

Fig. 2. Waveform encoding.

detection, and most of the detection time is consumed by the image creation. Therefore, it is necessary to utilize the sparsity characteristic of signals to encode waveforms into images, thus significantly improving the detection efficiency.

To improve the efficiency of image creation, a waveform encoding method is proposed. For a waveform signal displayed on a graph, its horizontal axis denotes the sampling time, and the vertical axis denotes the amplitude, which means that the sampling points are arranged in the graph according to the time sequence and amplitude. Suppose the signal $X = \{x_1, x_2, \cdots, x_p\}$ is normalized into [-1, 1], the generated binary image can be deemed as a matrix M, which has H rows and W columns, as shown in Fig. 2. Evidently, the horizontal axis corresponding to the sampling time is divided into W sections, and the vertical axis corresponding to the amplitude is divided into H sections.

For the i-th sampling section, the corresponding sampling points $x_{i'}$ can be obtained as (1).

$$\begin{cases} i_d = floor(i \times \dfrac{P}{W}) \\ i_u = ceil((i+1) \times \dfrac{P}{W}) \\ x_{i'} \ in \ X, \ i' \in [i_d, i_u] \\ i \in [1, \ W] \end{cases} \tag{1}$$

where P is total sampling points, and W is total sampling sections. *floor*(.) denotes round-down function, and *ceil*(.) denotes round-up function.

Subsequently, the extreme values of x in the i-th sampling section can be calculated as (2).

$$\begin{cases} x_{\max} = max\{x_{i'}\} \\ x_{\min} = min\{x_{i'}\} \end{cases}, \ i' \in [i_d, i_u] \tag{2}$$

where *max*(.) is used to determine the maximum value of x, and *min*(.) is utilized to obtain the minimum value of x.

For the j-th amplitude section, the width of each section can be obtained by using (3).

$$x_{\mathrm{w}} = \frac{2}{H} \tag{3}$$

The waveform in the i-th sampling section would pass through several amplitude sections. Wherein, the amplitude sections can be encoded as 1 if the value $x_{i'}$ is within the corresponding sections, otherwise the encoding value is 0, as shown in (4).

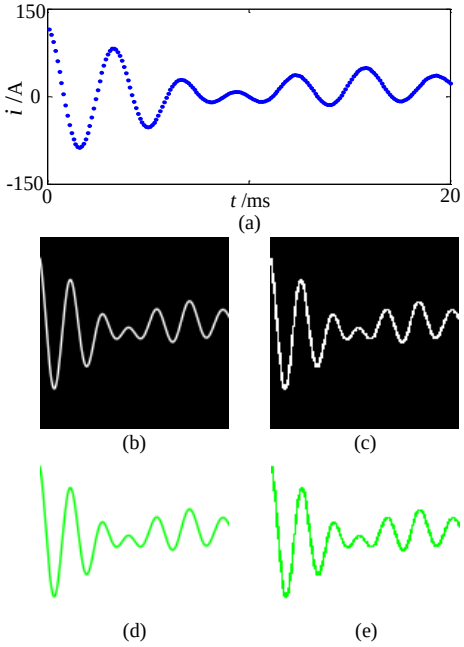

Fig. 3. Image creation (a) raw sampled data; (b) binary image generated by using 'plot' method; (c) binary image generated by using the proposed method; (b) colored image generated by using 'plot' method; (e) colored image generated by using the proposed method.

$$\begin{cases} j_d = round(\dfrac{H}{2}) - floor(\dfrac{x_{\max}}{x_{\mathrm{w}}}) \\ j_u = round(\dfrac{H}{2}) - floor(\dfrac{x_{\min}}{x_{\mathrm{w}}}) \\ M_{i,j'} = 1, \ j' \in [j_d, \ j_u] \\ M_{i,j''} = 0, \ j'' \notin [j_d, \ j_u] \end{cases} \tag{4}$$

where H is the total amplitude section, and *round*(.) denotes the round function.

After the above waveform encoding, each section can be encoded as 0 or 1, which implies that the value of $M_{i,j}$ can be obtained accordingly. Finally, the time-series signal X can be converted into a binary image with the size of $H \times W$. Similarly, the signal can also be converted into a colored image with three channels, where the encoding value 0 and 1 can be replaced by the vectors of length three.

To test the performance of the proposed waveform encoding method, an ideal ZSC signal is introduced [7] as follows:

$$\begin{cases} i(t) = i_1(t) + i_2(t) + i_3(t) + i_4(t) \\ i_1(t) = 10\cos(2\pi \times 50t + 60°) \\ i_2(t) = 40e^{-56t}\cos(2\pi \times 250t + 30°) \\ i_3(t) = 72e^{-102t}\cos(2\pi \times 315t) \\ i_4(t) = 10e^{-5.5t} \end{cases} \tag{5}$$

Suppose the sampling frequency is 10 kHz, raw ZSC, the generated binary images, and the generated colored images are shown in Fig. 3. Among them, the packaged function 'pyplot'

of 'matplotlib' base (version 3.5) in Python (version 3.7) is applied as the 'plot' method, and the images are generated on a computer with an Inter® Core™ processor i7-6700 (CPU), 3.40 GHz, 16.00 GB RAM.

Evidently, the images generated by using the encoding method are close to those obtained by using 'plot' method, where both images can effectively reflect the changing trends of raw signal. Besides, the encoding method only requires 2.49 ms for generating a binary image and 3.13 ms for generating a colored image, while the 'plot' method needs 23.68 ms and 23.11 ms, respectively. Therefore, the proposed encoding method can not only obtain the recognizable images, but also has high efficiency on generating images.

III. Faulty-Feeder Detection Method

According to analysis in Section II, the images can be generated quickly by using the proposed encoding method. Whereas, the reliability of detection results is another limiting factor for actual applications. To enhance the reliability, the fault signals are learned and recognized on the waveform scale, and the credibility of recognition results is further evaluated by using fault degree estimation. Furthermore, considering the future trend of protection devices towards to localization, it is necessary to enable faulty-feeder detection by using the local current transformer (CT) [27]. Compared with the existing detection methods based on the entire CTs, the detection methods based on the local CT can be directly applied to the existing feeder terminal units (FTU) or line protection devices without requirements for additional selection devices, which can significantly reduce the investment cost of substations. The detailed implementations are provided as follows.

A. Data Processing

The first half-cycle sampled data of ZSV on bus and local ZSC are collected and processed by using the amplitude normalization, as shown in (6).

$$\begin{cases} u_0^* = \dfrac{u_0(t)}{max(|\,u_0(t)\,|)} \\ i_{0n}^* = \dfrac{i_{0n}(t)}{max(|\,i_{0n}(t)\,|)} \end{cases}, t \in [t_f, t_f + \frac{T}{2}] \tag{6}$$

where u_0 is the sampled ZSV, and i_{0n} is the sampled ZSC of n-th feeder. u_0^* is the processed ZSV, and i_{0n}^* is the processed ZSC of n-th feeder. t_f is the fault time, and T is the cycle of fault signals.

After data processing, the ZSV and local ZSC are normalized into [-1, 1], and they can be superimposed in the same graph to generate the ZSV-ZSC image by using the proposed encoding method.

B. Image Creation

After data processing, the encoding matrix for the ZSV and ZSC can be obtained by waveform encoding, as shown in (7).

$$\begin{cases} M^{u} = e(u_0^*) \\ M^{i_n} = e(i_{0n}^*) \end{cases} \tag{7}$$

where $e(.)$ denotes the proposed encoding method, M^u is the encoding matrix of the ZSV on bus, and M^{i_n} is the encoding matrix of the local ZSC.

After waveform encoding, the binary image of local ZSC can be obtained. Subsequently, the encoding matrixes are utilized to generate the ZSV-ZSC image. Notably, because it is necessary to distinguish between the ZSV and ZSC in the ZSV-ZSC image, the required ZSV-ZSC image is saved in RGB form with three channels, which implies that the encoding value 0 and 1 in the matrixes need to be replaced by the vectors of length three. Wherein, the vector [0, 0, 0] denotes the black color, the vector [128, 0, 255] denotes the purple color, and the vector [255, 255, 0] denotes the yellow color. Finally, the matrix for the ZSV-ZSC image can be obtained by using (8).

$$\begin{cases} M_{i,j}^{u-i_n} = [255, 255, 0], \textit{if } M_{i,j}^{i_n} = 1 \\ M_{i,j}^{u-i_n} = [128, 0, 255], \textit{if } M_{i,j}^{u} = 1 \textit{ and } M_{i,j}^{i_n} = 0 \\ M_{i,j}^{u-i_n} = [0, 0, 0], \textit{if } M_{i,j}^{u} = 0 \textit{ and } M_{i,j}^{i_n} = 0 \end{cases} \tag{8}$$

Therefore, both the binary ZSC image and the colored ZSV-ZSC image can be generated, where the ZSV-ZSC image is recognized by using the waveform segmentation method.

C. Waveform Segmentation

To recognize the ZSV and ZSC on the waveform scale, it is necessary to conduct waveform segmentation on the generated ZSV-ZSC image. By making pixel-wise prediction on the image, both the complete waveform of ZSV and ZSC can be identified. Besides, each pixel in raw ZSC can be interpreted with different meanings, including 'faulty-feeder ZSC' and 'healthy-feeder ZSC'. Ideally, all the pixels in raw ZSC, which corresponds to the faulty feeder, are classified as 'faulty-feeder ZSC', and they are classified as 'healthy-feeder ZSC' in the ZSV-ZSC image corresponding to the healthy feeder.

In fact, the called waveform segmentation corresponds to semantic segmentation in computer vision tasks, where FCNs are widely applied in this field [33-34]. Commonly, FCNs utilize a set of convolutional layers, pooling layers, and upsampling layers to output a predicted map for the input image, where each pixel in the input image is classified. The segmentation process can be defined as (9).

$$V_{i,j} = F(M_{i,j}^{u-i_n}) \tag{9}$$

where $M_{i,j}^{u-i_n}$ denotes the pixel in the i-th sampling section and j-th amplitude section, and $V_{i,j}$ is the corresponding predicted label. $F(.)$ is the FCN model used for segmentation.

The combination of all the pixels with the same predicted label can consist of the segmented waveform with clear meaning. Among them, all the pixels classified as 'ZSV' correspond to the segmented ZSV, all the pixels classified as 'faulty-feeder ZSC' correspond to the segmented faulty-feeder ZSC, and all the pixels classified as 'healthy-feeder ZSC' correspond to the segmented healthy-feeder ZSC. In this paper, an efficient FCN is established for waveform segmentation, and the detailed implementation will be introduced in Section IV.

D. Fault Degree Estimation

Because there exist misclassifications of pixels in the output ZSV-ZSC images in practical applications, the segmented ZSC would be comprised of the segmented faulty-feeder ZSC and segmented healthy-feeder ZSC after waveform segmentation. To evaluate the credibility on the output results, the fault degree estimation is utilized by comparing the similarity between raw

ZSC and the segmented faulty-feeder ZSC. In this paper, the fault degree of each feeder is calculated by using (10), which corresponds to the dice coefficient [35] in semantic segmentation tasks.

$$FD_n = \frac{2\,|\,V^{i_n} \cap V^{s}\,|}{|\,V^{i_n}\,| + |\,V^{s}\,|} \tag{10}$$

where V^{i_n} is the set of pixels of the binary image of n-th ZSC generated by the M^{i_n}, and V^s is the set of pixels of the segmented faulty-feeder ZSC. $\cap$ denotes the intersection set between V^{i_n} and V^s, and FD_n is the calculated fault degree of the n-th feeder.

Because the segmented faulty-feeder ZSC and healthy-feeder ZSC can consist of the complete ZSC, the feeder can be identified as the faulty feeder if the segmented faulty-feeder ZSC accounts for the majority, where more than half of pixels in raw ZSC are classified as 'faulty-feeder ZSC'. According to (10), the threshold of fault degree can be set as 2/3 in theory. If the calculated fault degree is larger than 2/3, then more than half of the pixels are predicted as 'faulty-feeder ZSC', and the segmented ZSC is more likely to correspond to the ZSC of the faulty-feeder. Otherwise, the segmented ZSC can be identified as the healthy-feeder ZSC.

Notably, the fault degree of each feeder can be estimated on the waveform scale, which is not limited to certain fault features. Besides, the interpretability of the proposed learning-based method can be further enhanced by evaluating the recognition result based on the raw ZSC.

Finally, the fault degree of each feeder can be calculated, and the detection scheme can be constructed accordingly. For the line fault, the feeder whose fault degree is larger than 2/3 can be reliably determined as the faulty feeder, otherwise, it is judged as the healthy feeder. Regarding the bus fault, it can be deemed as a correct detection if each feeder is judged as healthy feeder.

E. Identification Steps

When an SPG fault occurs, it is necessary to sensitively capture the fault occurrence time while avoid disturbances. The triggering method is constructed based on the cooperation of differential criterion and RMS criterion [27], as shown in (11).

$$\begin{cases} |\,u_0(t_f) - u_0(t_f - T)\,| > u_{th} \\ U_0(t) > U_{th},\ t_f \le t \le t_d \\ |\,i_{0n}(t) - i_{0n}(t-T)\,| > i_{th},\ t_f \le t \le t_d \\ I_{0n}(t) > I_{th},\ t_f \le t \le t_d \end{cases} \tag{11}$$

where u_{th} is the threshold for the differential ZSV, U_0 is the calculated RMS value of ZSV, and U_{th} is the corresponding RMS threshold. i_{th} is the threshold for the differential ZSC, I_{0n} is the calculated RMS value of n-th ZSC, and I_{th} is the RMS threshold. t_f is the determined fault occurrence time, and t_d is the opening time of the triggering method.

The fault time can be sensitively captured by the differential criterion of the ZSV, and the other criterions are used for confirmation. Further identification schemes are triggered only if all the criterions meet the requirements. Besides, the RMS criterion of ZSV needs to be continuously satisfied before final isolation of faulty feeder, and it can avoid device misoperation caused by normal disturbances, such as capacitor switching, load switching, and inrush currents [4], where the ZSVs are small and decay rapidly under disturbances.

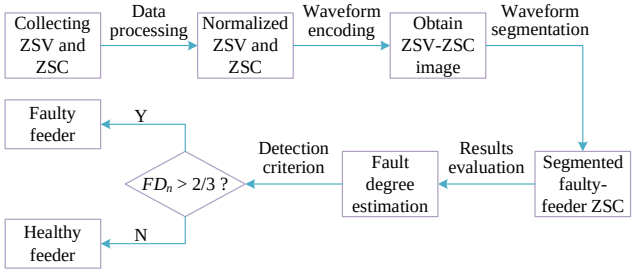

Fig. 4. Identification process of the FCN-based method.

After the SPG faults are confirmed, the specific steps of the proposed FCN-based method are shown in Fig. 4.

Step 1: Data processing: Collect the first half-cycle sampled data of ZSV on bus and local ZSC, and then, process the sampled data by using the amplitude normalization.

Step 2: Waveform encoding: Encode the waveform of ZSV and ZSC, and obtain the ZSV-ZSC image.

Step 3: Waveform segmentation: Recognize the ZSV-ZSC image by using the established FCN, and obtain the segmented waveform corresponding to the faulty-feeder ZSC.

Step 4: Results evaluation: Calculate the fault degree FD_n of feeder n by comparing the similarity between the segmented faulty-feeder ZSC and raw ZSC.

Step 5: Detection criterion: If the calculated FD_n is larger than 2/3, the feeder n is selected as the faulty feeder. Otherwise, the feeder n is identified as the healthy feeder.

IV. Theory of Two-Path FCN

A. Model of Two-Path FCN

In this paper, an FCN network with two paths, called two-path FCN, is established, as shown in Fig. 5. The first path is an FCN with multi-scale fusion structures, which is used for global segmentation prediction. The second one is a classification path that produces an overall prediction on the input image. The shared network of the two paths is a base recognition model by using ResNet [36] in the encoder stage.

In the encoder stage, the lower layers have finer spatial information and poor semantic consistency, while the higher layers have strong semantic consistency and coarse spatial information. For the segmentation path, it is necessary to combine their advantages by using the skip structures in the decoder stage. That is to say, the output feature maps in the higher layers are upsampled and added with those in the corresponding lower layers. Besides, the feature maps in the decoder stage are upsampled by using different scales and are fused by using (12), where the refinement residual block (RRB) [34] is utilized to decrease the channel number of feature maps in the upsampling process.

$$P^s = up^{8x}(f^{2-nd}) + up^{4x}(f^{3-rd}) + up^{2x}(f^{4-th}) \tag{12}$$

where $f^{2\text{-nd}}$, $f^{3\text{-rd}}$, and $f^{4\text{-th}}$ are the output feature maps of the second RRB layer, the third RRB layer, and the fourth RRB layer, respectively. $up^{2x}(.)$, up^{4x} (.), and up^{8x} (.) denote the upsampling function with 2 scale factor, 4 scale factor, and 8 scale factor, respectively. P^s is the predicted map in the segmentation path.

The loss function of the first path can be calculated as:

$$L_1(P^s, G) = -\sum_i (g_i \log p_i^s + (1 - g_i)\log(1 - p_i^s)) \tag{13}$$

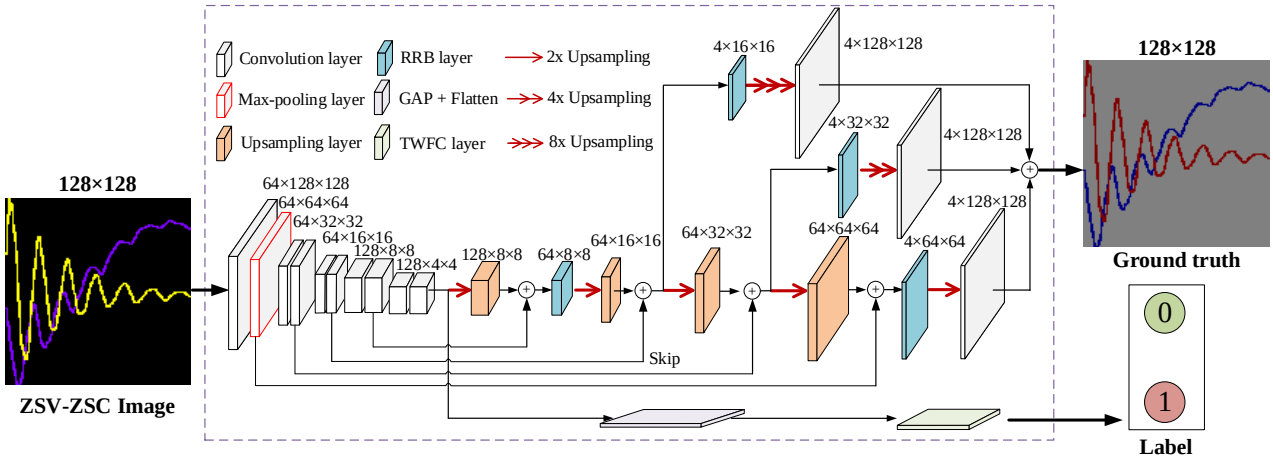

Fig. 5. Structure of two-path FCN.

where p_i^s is the probability of a pixel i in the predicted map P^s, and g_i is the true value in the corresponding ground truth map G. L_1 is the calculated loss function of the first path.

For the classification path, the last layer in the encoder stage is stacked with a global average pooling (GAP) layer and a two-way fully-connected (TWFC) classification layer. Since the classification path can make a prediction on the whole image scale, it can cooperate the segmentation path for the optimal prediction. The loss function of the second path is expressed as:

$$L_2(P^c, Y) = -\frac{1}{N}\sum_i (y_i \log p_i^c + (1-y_i)\log(1-p_i^c)) \quad (14)$$

where p_i^c is the probability classified as 'faulty feeder' of the i-th image, and y_i the true label of the i-th image.

Finally, the output results of the two paths are merged, and the final loss function can be obtained by using (15).

$$L = L_1(P^s, G) + \lambda L_2(P^c, Y) \quad (15)$$

where the hyper parameter λ is used to balance the loss of two paths, and it can be changed accordingly in the iteration epochs.

To sum up, the first path of the FCN, which corresponds to the path of semantic segmentation, can have detailed understanding on the waveforms by making pixel-wise prediction on the ZSV-ZSC images; the second path used for classification on the whole image can obtain an overall prediction on the input image, where the label is 1 if the image contains the faulty-feeder current, otherwise, the label is 0. Notably, for the faulty-feeder detection, only the output of the first path is utilized in the test process.

B. *Training of Two-Path FCN*

To obtain the adequate fault data for training the established two-path FCN, SPG faults are simulated by using PSCAD software. Three distribution network models are established, and they contain four feeders, where the feeder length is 10 km, 20 km, 30 km, and 40 km, respectively. Among them, the parameters of the overhead lines are: $R_1 = 0.17$ Ω/km, $L_1 = 1.21$ mH/km, $C_1 = 0.0097$ μF/km, $R_0 = 0.23$ Ω/km, $L_0 = 5.48$ mH/km, and $C_0 = 0.006$ μF/km, and the parameters of the cable lines are: $R_1 = 0.098$ Ω/km, $L_1 = 0.274$ mH/km, $C_1 = 0.351$ μF/km, $R_0 = 0.246$ Ω/km, $L_0 = 0.955$ mH/km, and $C_0 = 0.166$ μF/km. Both neutral point ungrounded mode (model 1) and resonant grounded mode (model 2 and model 3) are considered.

TABLE I
FAULT CONDITIONS IN TRAINING DATASET

Fault location	D	θ_f / °	R_f / Ω	Sample number
l_1–l_4 (Three models)	10%, 50%, 90%	0~360 per 22.5	20, 100, 500, 1000	2,448
Bus (Three models)	/	0~360 per 7.2	20, 100, 500, 1000	612

Furthermore, the training model 1 and model 2 comprises of overhead lines, while the training model 3 consists of cable lines (10 km and 20 km) and overhead lines (30 km and 40 km). Various fault conditions are considered in the production of training dataset, including different fault location, fault distances D, initial phases θ_f, and grounding resistances R_f, as summarized in Table I. The sampling frequency is 20 kHz.

Notably, the training dataset is easy to obtain by using PSCAD software. Besides, the training dataset only considers common fault conditions, while the complex fault conditions, such as intermittent arc grounding faults and nonlinear high impedance faults (HIFs), are directly utilized to verify the detection performance in the test process.

For the training dataset, totally 12,240 (2448 × 4 + 612 × 4) sets of ZSV-ZSC images are obtained, and they are flipped vertically in the training process. The two-path FCN model is trained on a computer with an Inter® Core™ processor i7-6700 (CPU), 3.40 GHz, 16.00 GB RAM, and NVIDIA GeForce GTX 1050. After the established model is trained, only the output of the first path is utilized in the following test process.

V. SIMULATION AND VERIFICATION

To verify the detection performance, both simulation data and practical data are utilized as the test dataset in this study, including fault data obtained from PSCAD simulation, RTDS hardware-in-the-loop (HIL) test system, field test, and practical distribution networks. Notably, the distribution networks in the test dataset are completely different from those in the training dataset, and the fault scenarios are more complex in the test process. Moreover, to evaluate the real-time performance of the proposed FCN-based method, a basis hardware platform, called NVIDIA Jetson AGX Xavier equipped with graphics processing units (GPUs), is used in the following test, and all the detection process was implemented in the established PIL experimental system.

TABLE II
SPECIFICATIONS OF JETSON AGX XAVIER

Hardware	Specifications
GPU	512-core Volta GPU with Tensor Cores
CPU	8-core ARM v8.2 64-bit CPU, 8 MB L2 + 4 MB L3
Video memory	32 GB 256-Bit LPDDR4x | 137 GB/s
Storage	32 GB eMMC 5.1
DL accelerator	(2x) NVDLA Engines
Vision accelerator	7-way VLIW Vision Processor
Encoder/Decoder	(2x) 4Kp60 | HEVC/(2x) 4Kp60 | 12-Bit Support
Mechanical	105 mm x 105 mm x 65 mm

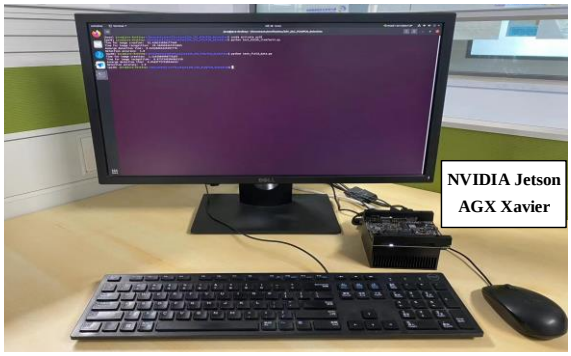

Fig. 6. PIL experimental system.

A. PIL Experimental System

As the AI-powered autonomous machines, the NVIDIA Jetson AGX Xavier modules have the potential to be equipped in the future applications due to the superior AI performance [37]. The NVIDIA Jetson boards have a comprehensive set of tools for AI computing purposes, including a power-efficient dedicated deep learning (DL) accelerator, CPU, and GPU. In this study, the proposed method based on the trained FCN model was deployed in a NVIDIA Jetson AGX Xavier module, and the detailed specifications are listed in Table II.

The experimental environment of the Jetson module is Ubuntu 20.04, Python 3.8, and Pytorch 1.12. The embedded Jetson device is connected to a DELL monitor and is controlled by a mouse and keybord. The physical connection of the established PIL experimental system is shown in Fig. 6.

B. Fault Data Obtained from PSCAD Simulation

The established radial distribution network comprises of six feeders in PSCAD simulation, and three DGs are connected to the grid through switches S_1, S_2, and S_3, as shown in Fig. 7. Among them, the parameters of the overhead lines are as follows: R_1 = 0.33 Ω/km, L_1 = 1.31 mH/km, C_1 = 7.0 nF/km, R_0 = 1.041 Ω/km, L_0 = 3.96 mH/km, and C_0 = 4.0 nF/km, and the parameters of cable lines are as follows: R_1 = 0.0791 Ω/km, L_1 = 0.264 mH/km, C_1 = 373.0 nF/km, R_0 = 0.227 Ω/km, L_0 = 0.926 mH/km, and C_0=166.0 nF/km. The power consumed by each load is 0.959+j0.313 MVA, and the DGs are PV farms, where the total power generated by each DG is 2.272+j0.860 MVA and the detailed converter structure and control strategy can be found in [38]. Furthermore, the sampling frequency in PSCAD simulation is just 10 kHz, which is only half of that in the training dataset, and the ratio of CTs is 50A/1A.

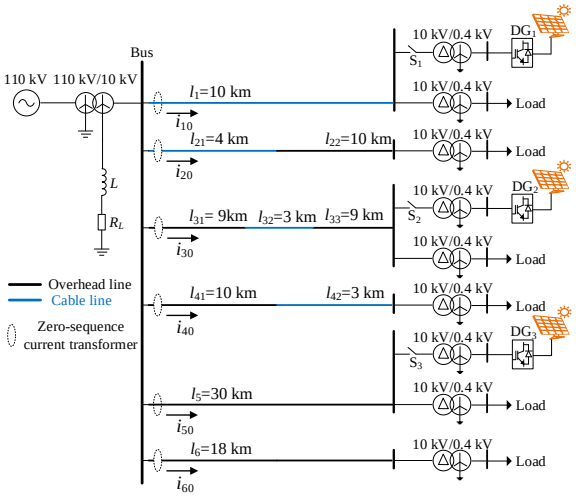

Fig.7. Distribution network with DGs connection.

TABLE III
FAULT SCENARIOS IN PSCAD SIMULATION

Fault conditions	Parameters
Fault location	l_1 ~ l_6, Bus
D / km	5 (l_1), 4 (l_2), 12 (l_3), 10 (l_4), 20 (l_5), 9 (l_6), Bus
θ_f / °	0~360 per 18
R_f / Ω	1 / 10 / 50 / 200 / 800 / 1300 / 2000
Sample number	1,029

To verify the generalization capability, the SPG fault conditions are changed, including different fault locations, fault distances D, initial phases θ_f, and grounding resistances R_f. Totally 1,029 sets of fault data are obtained in PSCAD simulation, where 882 (6 × 21 × 7) sets of data are line faults and 147 (21 × 7) sets of fault data are bus faults. The detailed fault scenarios are summarized in Table III.

The obtained fault data is processed by using the Jetson module, including waveform encoding, image creation, and waveform segmentation. Several generated ZSV-ZSC images and the corresponding segmentation results are shown in Fig. 8, where Gaussian white noise with the signal-to-noise-ratio (SNR) of 10 dB was added to the sampled ZSCs in Fig. 8 (d), Fig. 8 (e), and Fig. 8 (f) and each DG is connected to the network, and the complete waveforms of ZSV and ZSCs are shown in Fig. 9. The horizontal axis in the obtained ZSV-ZSC images denotes the sampling time (the first half-cycle), and the vertical axis denotes the normalized amplitude ([-1, 1]). For the segmentation results, each pixel in the ZSV-ZSC images is classified, where the label of 'faulty feeder' is marked in red and the label of 'healthy feeder' is marked in green.

Evidently, the ZSVs and ZSCs have changing fault features under different fault conditions. Compared with the ZSVs, the ZSCs have more complex fault transients especially under noise interferences, leading to varied characteristics of oscillations and attenuation. Besides, there are large differences of resonant frequencies between ZSCs of different feeders even under the same fault conditions. Consequently, the varied fault characteristics would make it rather difficult to detect the specific faulty feeder. However, the trained FCN model can always identify the faulty feeder with high reliability. For the line faults, the estimated fault degree of the faulty feeder is 0.97,

0.99, 0.96, 0.95, 0.96, and 0.93, respectively, and the fault degree of the healthy feeder are 0.00, 0.00, 0.00, 0.00, 0.00, and 0.00, respectively. Regarding the bus faults, the calculated fault degrees in Fig.8 (g) and Fig.8 (h) are 0.00, 0.00, 0.00, and 0.00, respectively. Therefore, the FCN-based method can not only distinguish between line faults and bus faults, but also can reliably identify the faulty feeder and the healthy feeder.

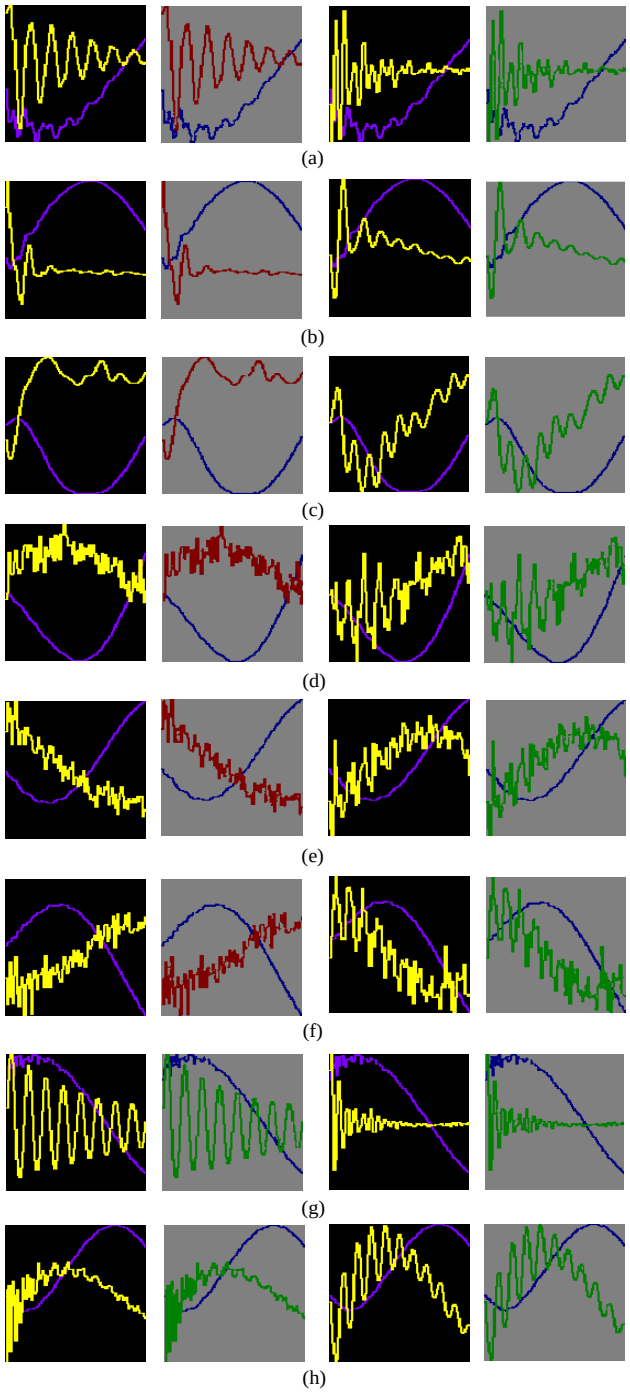

Fig.8. ZSV-ZSC images and the corresponding segmentation results in PSCAD simulation (a) fault in feeder 1, 36°, 1 Ω, the images correspond to faulty feeder 1 and healthy feeder 5, respectively; (b) fault in feeder 2, 162°, 10 Ω, faulty feeder 2, healthy feeder 3; (c) fault in feeder 3, 342°, 50 Ω, faulty feeder 3, healthy feeder 4; (d) fault in feeder 4, 18°, 1300 Ω, faulty feeder 4, healthy feeder 3; (e) fault in feeder 5, 90°, 800 Ω, faulty feeder 5, healthy feeder 1; (f) fault in feeder 6, 252°, 2000 Ω, faulty feeder 6, healthy feeder 4; (g) fault in Bus, 234°, 1 Ω, healthy feeder 3, healthy feeder 5; (h) fault in Bus, 144°, 200 Ω, healthy feeder 2, healthy feeder 4.

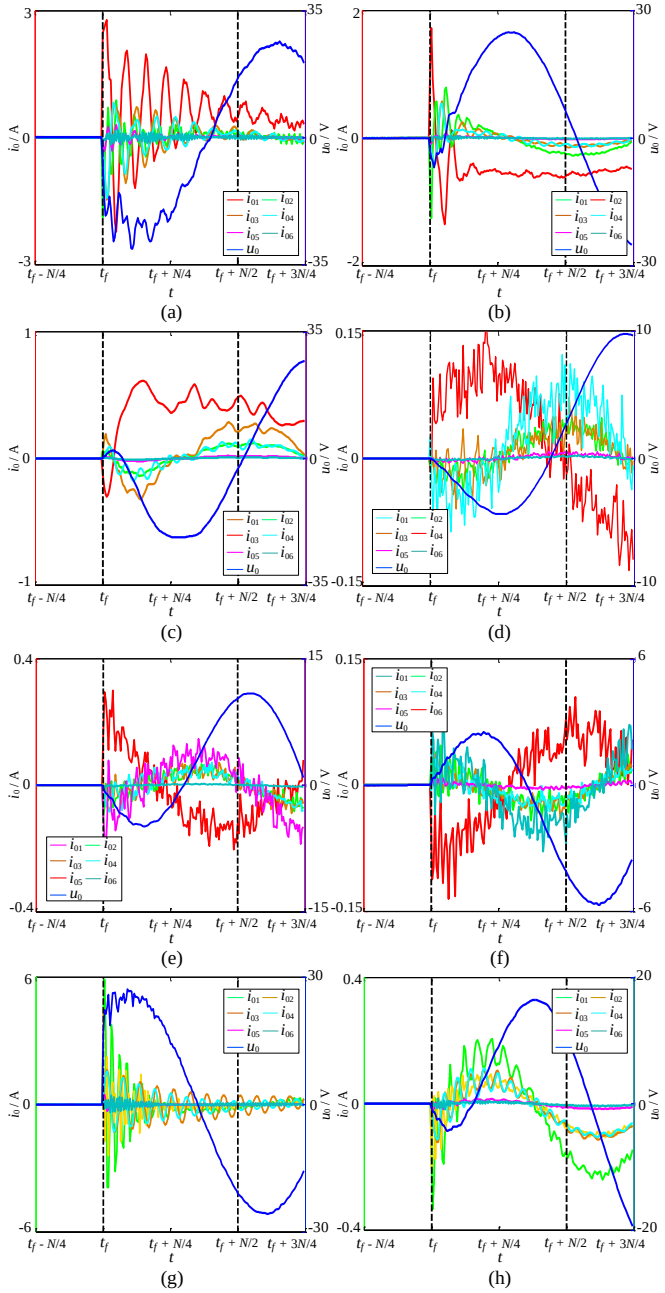

Fig.9. Complete waveforms of ZSV and ZSCs corresponding to Fig. 8.

(1) Adaptability Analysis on Compensation Degrees: Because the ZSCs may vary under different compensation degrees, this study considers 3%, 6%, 10%, and 15% overcompensation degrees, respectively, and each DG is connected to the distribution networks in the test process. The detailed fault conditions are shown in Table III, and totally 4,116 (1,029 × 4) sets of fault data are obtained. The detection results under different compensation degrees (ρ) are shown in Table IV. Evidently, the proposed method can still have 100% detection accuracy when the degree of compensation changes. This is mainly because the arc suppression coil is designed to compensate the steady-state ZSC of the faulty feeder in the fundamental frequency, and the faulty-feeder ZSC in the first half-cycle and the healthy-feeder ZSCs are hardly affected [26]. Therefore, the proposed method has good adaptability to varying parameters of the arc suppression coil.

TABLE IV
DETECTION ACCURACY UNDER DIFFERENT COMPENSATION DEGREES

Fault type	ρ = 3%	ρ = 6%	ρ = 10%	ρ = 15%
Line fault (882)	100%	100%	100%	100%
Bus fault (147)	100%	100%	100%	100%

TABLE V
DETECTION ACCURACY UNDER DIFFERENT CONNECTION AND CAPACITIES OF DGS

Switches	Capacity / MVA	Line fault (882)	Bus fault (147)
Open	/	100%	100%
Closed	0.61	100%	100%
	1.21	100%	100%
	1.82	100%	100%
	2.43	100%	100%

TABLE VI
DETECTION ACCURACY UNDER DIFFERENT THRESHOLDS

Fault type	α = 0.2	α = 0.4	α = 0.6	α = 2/3	α = 0.8
Line fault (882)	100%	100%	100%	100%	100%
Bus fault (147)	100%	100%	100%	100%	100%

(2) Adaptability Analysis on DGs Connection: Although the DGs are connected to the network via isolation transformers with Yg/△ winding configuration, which implies that the ZSCs can only form circulation in △ but cannot flow out of the transformers, the harmonics generated by DGs in the positive-sequence network may affect the zero-sequence components as the three-sequence networks are connected in series at the fault point [15]. Consequently, it is necessary to verify the detection performance under distribution networks with and without DGs connection. Furthermore, there may be larger harmonics when the capacity of DGs increases.

To evaluate the detection performance under different connections and capacities of DGs, the switches are open and closed, respectively, and varied capacities of each DG, such as 0.61 MVA, 1.21 MVA, 1.82 MVA, and 2.43 MVA, are considered. Totally 5,145 (1,029 × 5) sets of fault data are obtained, and the detection results are shown in Table V. As shown in Table V, the proposed method is immune from the different connections and capacities of DGs, and it can always distinguish between bus faults and line faults and identify the faulty feeder under line faults accurately. Therefore, the proposed method can be applied to the faulty-feeder detection under distribution networks with and without DGs connection.

(3) Sensitivity Analysis on Thresholds: To validate the sensitivity of the proposed method on different thresholds, the threshold (α) of fault degree is set to 0.2, 0.4, 0.6, 2/3, and 0.8, respectively. Among them, the overcompensation degree of the network is 6%, the capacity of DGs is 2.43 MVA, and all the switches are closed. The detection results under different thresholds are shown in Table VI.

As shown in Table VI, the proposed method still has 100% detection accuracy under different thresholds. This is mainly because the proposed two-path FCN has high segmentation accuracy, and most of pixels in raw ZSC waveform can be classified as 'faulty-feeder ZSC' for the faulty-feeder ZSV-ZSC image, while most of pixels in raw ZSC waveform can be classified as 'healthy-feeder ZSC' for the healthy-feeder ZSV-ZSC image. That is, the calculated fault degree of the faulty feeder is close to 1, while the calculated fault degree of the healthy feeder is close to 0, and consequently, the faulty feeder and healthy feeder can still be distinguished with high accuracy under different thresholds. In this study, considering the misclassification of pixels in practical applications, the threshold should be designed in a scientific way, and it needs to be set to 2/3 in theory according to (10).

TABLE VII
DETECTION ACCURACY IN PSCAD SIMULATION

Fault type	Paper [7]	Paper [39]	Proposed method
Line fault (882)	82.20%	85.03%	99.77%
Bus fault (147)	×	87.76%	100%

(4) Comparison with Existing Methods: To verify the superiority of the proposed method, the detection performance is compared with the existing methods [7] [39]. Wherein, paper [7] identified the faulty feeder based on the multi-feature fusion, including transient energy, kurtosis, and cross-correlation distance (CCD), which belongs to analysis-based methods, and paper [39] utilized continuous wavelet transform to obtain the time-frequency images and constructed the detection scheme based on the image recognition by using CNN, which corresponds to learning-based methods. In this section, each DG with 2.43 MVA is connected to the network, which implies that all the switches are closed, and the overcompensation degree is set to 6%. Furthermore, Gaussian white noise with SNR of 10 dB was added to the sampled ZSCs when SPG faults with 800 Ω, 1300 Ω, and 2000 Ω occurred. The obtained 1,029 sets of fault data are utilized for performance evaluation, and the detection accuracy is shown in Table VII.

Evidently, paper [7] has unsatisfactory detection accuracy for identifying the faulty feeder. This is mainly because the inherent limitations of multi-feature fusion hinder the detection performance: the miscalculations in the three extracted features may result in failure for faulty-feeder detection. Misjudgments would occur if there are miscalculations of two features, or even one feature is greatly miscalculated. For instance, the healthy feeder 1 has the largest values of calculated kurtosis and CCD in Fig. 9 (d), and it is misjudged as the faulty feeder. Especially, the calculated kurtosis of the healthy feeder 1 is 0.23 in Fig. 9 (e), which is greatly larger than that of the faulty feeder 5 (0.14), thus leading to the misjudgment. Furthermore, paper [7] directly selects the feeder with the maximum fusion results as the faulty feeder, which implies that it cannot identify the bus faults. Compared with the paper [7], paper [39] has higher faulty-feeder detection accuracy, and it can also identify the bus faults. However, since paper [39] recognizes the time-frequency image of each feeder, which implies that it fails to consider the correlation between different feeders, the changing fault features of ZSCs result in poor robustness under different fault scenarios, especially for strong noise interference. In contrast, the proposed method identifies fault signals on the waveform scale and has detailed understanding on waveforms, and it has high detection accuracy both for line faults and bus faults, thus demonstrating its strong generalization capability.

TABLE VIII
DETECTION TIME IN PSCAD SIMULATION

Average Time	Paper [7]	Paper [39]	Proposed method
Time window (ms)	20	10	10
Image creation (ms)	/	259.36	10.68
Image recognition / Detection (ms)	8.66	7.84	5.91
Total (ms)	28.66	277.20	26.59

Moreover, the detection time of each method is shown in Table VIII. For the paper [7], the time consumed to detect an SPG fault in the embedded device is 28.66 ms, and it has good detection efficiency. Regarding the paper [39], it even requires a total of 277.20 ms on average to conduct an SPG detection, where generating the time-frequency images is quite time-consuming. In contrast, an SPG fault detection can be completed within 26.59 ms by using the proposed method, including 10.68 ms for image creation and 5.91 ms for image recognition. Notably, the proposed method utilizes the local ZSC for detecting the faulty feeder, which implies that each feeder is identified in parallel. Therefore, owing to the proposed waveform encoding method and detection scheme based on the local ZSC, the proposed method has superior detection efficiency and has the potential for real-time applications.

C. *Fault Data Obtained from RTDS HIL Test System*

Because the PSCAD software is a digital simulation environment without real hardware sections of detection devices, this study establishes the RTDS HIL test system, as shown in Fig. 10. The test system contains four sections: distribution system modeling, power amplifier, protection device, and fault recorder. Among them, the digital signals generated by the established model are converted into analog signals by real power amplifier, and they are sampled at 12 kHz by using practical fault recorder with 100A/1A measurement ratio of CTs, considering system noise interference and actual measurement errors.

The established distribution network in RTDS test system consists of two Buses and 15 feeders, as shown in Fig. 11, and its grounding modes can be changed through the grounding transformer. The detailed feeder parameters and fault scenarios are shown in Table IX and Table X, respectively, and totally 69 sets of fault data are obtained, where 31 sets of SPG faults occurred in the ungrounded network and the remaining faults occurred in the resonant grounding network.

It is noteworthy that the SPG faults simulated in the RTDS test system contains the arc grounding events, while they are not considered in the training dataset. Furthermore, HIFs with 1 kΩ are also considered in the test process. Typical generated ZSV-ZSC images and the corresponding segmentation results are shown in Fig. 12, and the complete waveforms can be found in Fig. 13.

As shown in Fig. 12 and Fig. 13, the ZSCs become zero when the arcs are extinguished, and then they would go into new oscillation states when the arcs reburn. Compared with the oscillations and attenuation characteristics under traditional fault scenarios, ZSCs may have additional distortions in

Fig. 10. RTDS HIL test system.

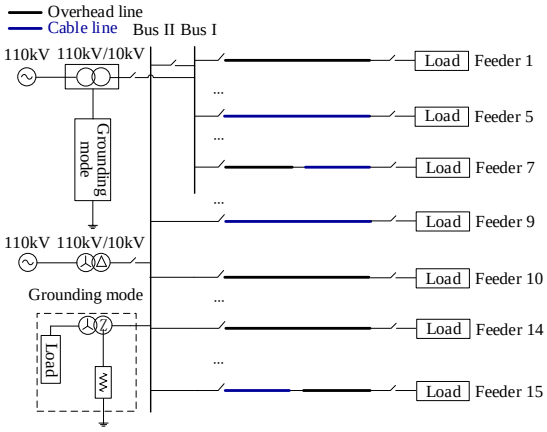

Fig. 11. Distribution network established in RTDS simulation.

TABLE IX
PARAMETERS OF FEEDERS IN RTDS SIMULATION

Type	Phase-sequence	R (Ω / km)	L (mH / km)	C (μF / km)
Overhead line	Positive	0.33 / 0.45	1.31 / 1.31	0.007 / 0.007
	Zero	1.04 / 1.44	3.96 / 4.05	0.004 / 0.004
Cable line	Positive	0.08 / 0.10	0.26 / 0.27	0.373 / 0.351
	Zero	0.23 / 0.25	0.93 / 0.96	0.166 / 0.166

TABLE X
FAULT SCENARIOS IN RTDS SIMULATION

Fault conditions	Parameters
Fault location	Feeder 1, 5, 7, 9, 10, Bus
θ_f / °	30, 60, 90, 120, 123, 150, 180, 210, 243, 270, 330
R_f / Ω	1.1, 5.82, 10, 240, 1000
Arc grounding	Yes / No
Sample number	69

waveforms, thus causing great challenges for subsequent faulty-feeder detection. However, the trained FCN model can still recognize the ZSV-ZSC images with high segmentation accuracy, where the faulty-feeder ZSC and healthy-feeder ZSC can be clearly distinguished. Finally, for the line faults shown in Fig. 12 (a), Fig. 12 (b), Fig. 12 (c), Fig. 12 (e), Fig. 12 (f), and Fig. 12 (g), the calculated fault degree of the faulty feeder is 0.99, 0.99, 0.98, 0.97, 0.98, and 0.99, respectively, and the calculated fault degree of the healthy feeder is 0.00, 0.00, 0.00, 0.00, 0.00, and 0.00, respectively. Regarding the bus faults shown in Fig. 12 (d) and Fig. 12 (h), the calculated fault degrees

This article has been accepted for publication in IEEE Transactions on Smart Grid. This is the author's version which has not been fully edited and content may change prior to final publication. Citation information: DOI 10.1109/TSG.2023.3243026

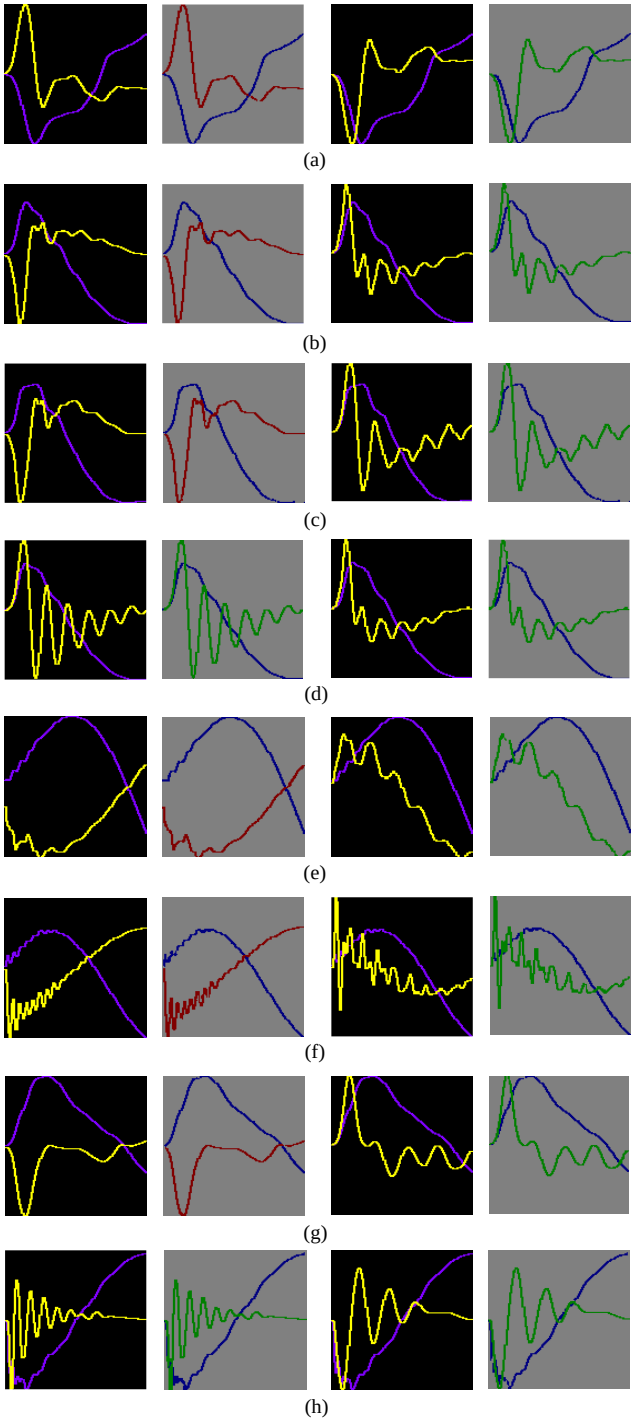

Fig.12. ZSV-ZSC images and the corresponding segmentation results in RTDS simulation (a) arc grounding fault in feeder 1, 270°, 10 Ω, ungrounded network, the two images correspond to faulty feeder 1 and healthy feeder 7, respectively; (b) arc grounding fault in feeder 7, 30°, 10 Ω, ungrounded network, the two images correspond to faulty feeder 7 and healthy feeder 3, respectively; (c) arc grounding fault in feeder 9, 30°, 10 Ω, ungrounded network, the two images correspond to faulty feeder 9 and healthy feeder 14, respectively; (d) arc grounding fault in Bus, 30°, 10 Ω, ungrounded network, the two images correspond to healthy feeder 1 and 6, respectively; (e) HIF with 1 kΩ in feeder 1, 330°, resonant grounding network, the two images correspond to faulty feeder 1 and healthy feeder 7, respectively; (f) HIF with 1 kΩ in feeder 5, 150°, resonant grounding network, the two images correspond to faulty feeder 5 and healthy feeder 3, respectively; (g) arc grounding fault in feeder 9, 243°, 10 Ω, resonant grounding network, the two images correspond to healthy feeder 9 and 12, respectively; (h) fault in Bus, 90°, 10 Ω, resonant grounding network, the two images correspond to healthy feeder 3 and 7, respectively.

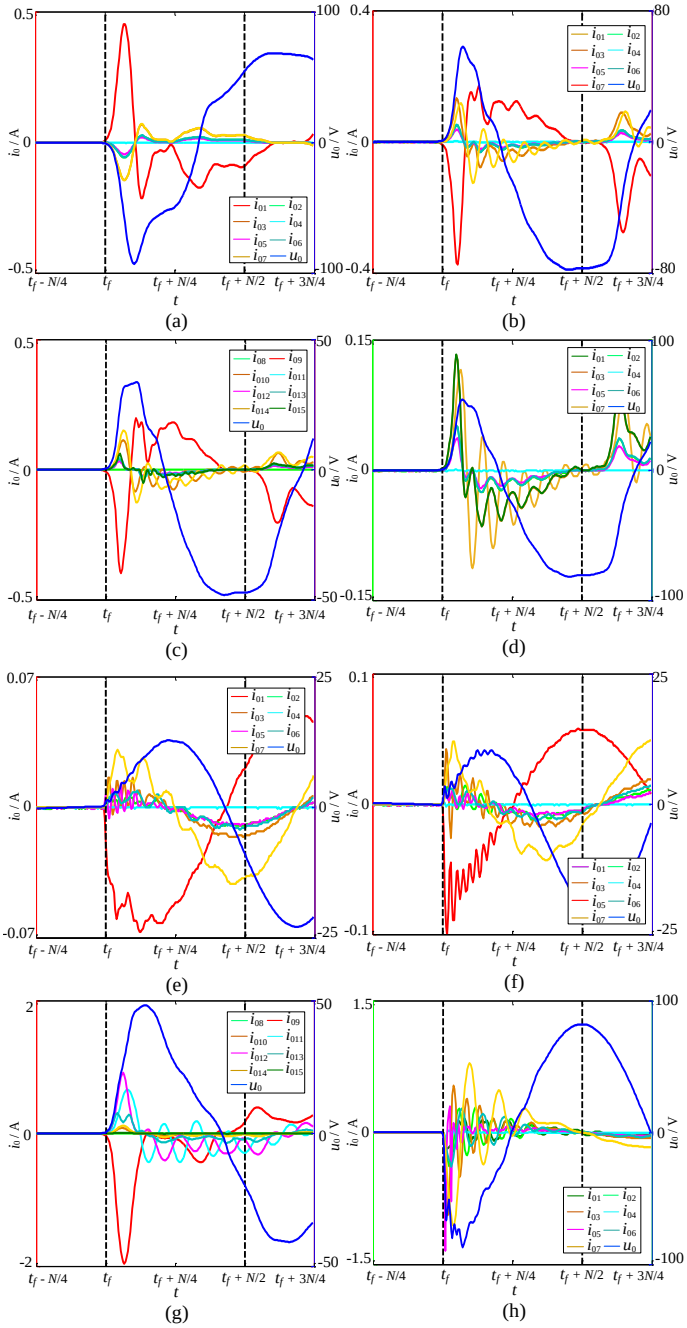

Fig.13. Complete waveforms of ZSV and ZSCs corresponding to Fig. 12.

are 0.00, 0.00, 0.00, and 0.00, respectively. Therefore, the proposed FCN-based method can always recognize the faulty feeder and healthy feeder with good reliability.

The detailed detection results of different methods are shown in Table XI. Due to the distortions in waveforms and changes of sampling frequency, the time-frequency characteristics of ZSCs are different from those in the training dataset, and the detection accuracy of paper [39] is even much worse than that of paper [7]. Furthermore, paper [7] would misjudge the bus faults as line faults in the detection process. In contrast, the proposed method can always accurately detect the faulty feeder under various fault scenarios, and it can also have optimal computation speed. Therefore, the proposed method has excellent detection performance in the RTDS HIL test system.

TABLE XI
DETECTION RESULTS IN RTDS HIL TEST SYSTEM

Detection	Grounding mode	Paper [7]	Paper [39]	Proposed method
Accuracy	Ungrounded	93.55%	83.87%	100%
	Resonant grounding	94.74%	68.42%	100%
Average Time	Ungrounded	34.23 ms	322.09 ms	25.71 ms
	Resonant grounding	33.36 ms	295.07 ms	26.37 ms

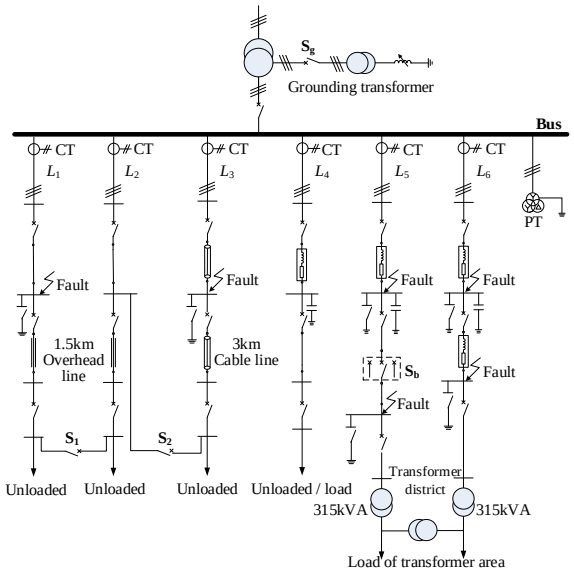

Fig.14. Structure of the field test.

D. *Fault Data Obtained from Field Test*

To verify the adaptability in practical applications, we conducted the field test at Luohe substation of Henan in China. The distribution network structure is shown in Fig. 14. In Fig. 14, there are six feeders, named L_1 - L_6, including three practical feeders L_1 - L_3 and three analog feeders L_4 - L_6. The neutral point of power transformer is connected to the ground through a grounding transformer, and the grounding mode can be changed through the switch S_g.

Compared with the fault conditions simulated in PSCAD, the actual SPG fault scenarios are more complex, and the recorded data contains real measurement errors and noise interference. Especially, actual SPG faults are usually accompanied by intermittent arc grounding events, and HIFs occasionally occur when a primary conductor is connected to high resistive mediums, such as wet grass, tree, and concrete, thus leading to considerable nonlinearity and randomness of fault features.

Notably, these new fault scenarios would cause great challenges for the learning-based methods if they fail to learn the essential fault characteristics from the training dataset.

In field test, arc grounding faults under different arc conditions are simulated by setting varied discharge distances. Besides, single-phase line-broken faults are also conducted, and the grounding medium is the concrete floor. Furthermore, CTs were installed at the beginning of feeders, and the corresponding measurement ratios are 100A/5A. The fault data was collected by using real fault recorder, where the sampled data of ZSV on bus and ZSCs of feeders is recorded, and the sampling frequency is 20 kHz.

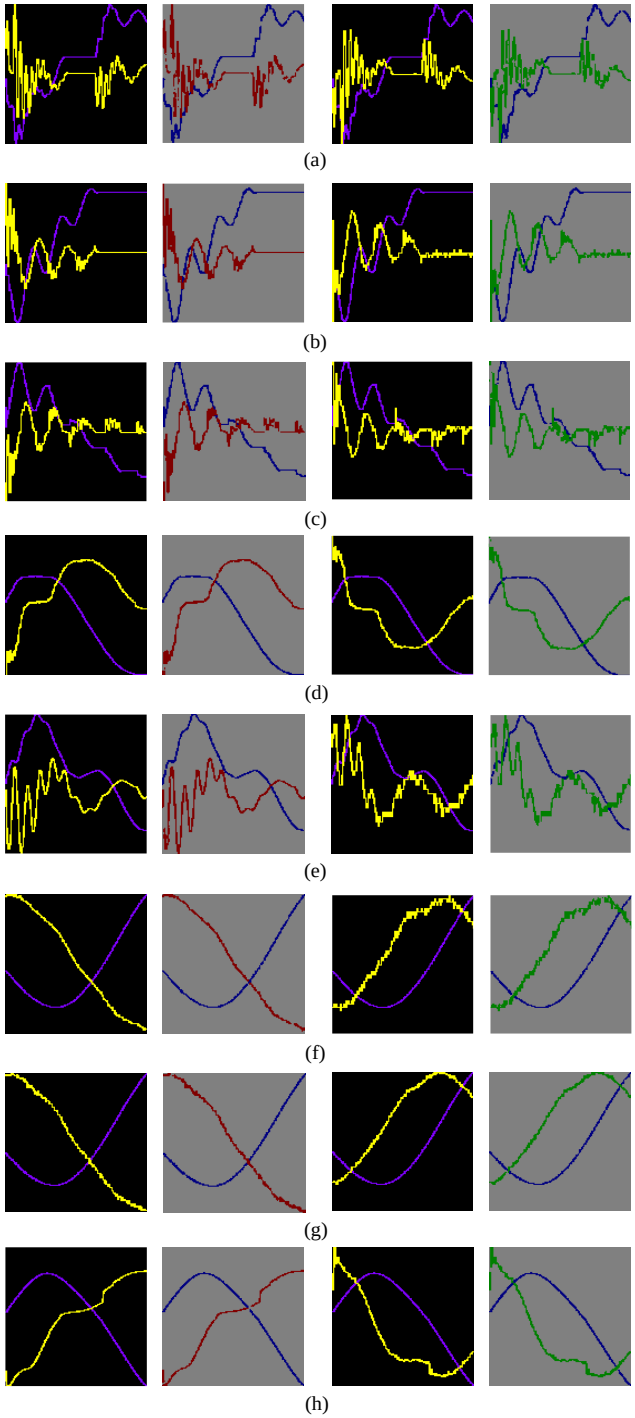

Fig.15. ZSV-ZSC images and the corresponding segmentation results in field test (a) transient arc grounding fault, S_g is open, the two images correspond to faulty feeder 1 and healthy feeder 2, respectively; (b) steady arc grounding fault, S_g is open, the two images correspond to faulty feeder 4 and healthy feeder 5, respectively; (c) arc grounding fault occurred in cable line, S_g is open, the two images correspond to faulty feeder 3 and healthy feeder 6, respectively; (d) single-phase line-broken fault, S_g is open, the two images correspond to faulty feeder 2 and healthy feeder 4, respectively; (e) transient arc grounding fault, S_g is closed, the two images correspond to faulty feeder 1 and healthy feeder 6, respectively; (f) HIFs with 1 kΩ, S_g is closed, the two images correspond to faulty feeder 2 and healthy feeder 1, respectively; (g) HIFs with 2 kΩ, S_g is closed, the two images correspond to faulty feeder 2 and healthy feeder 3, respectively; (h) single-phase line-broken fault, S_g is closed, the two images correspond to faulty feeder 2 and healthy feeder 1, respectively.

This article has been accepted for publication in IEEE Transactions on Smart Grid. This is the author's version which has not been fully edited and content may change prior to final publication. Citation information: DOI 10.1109/TSG.2023.3243026

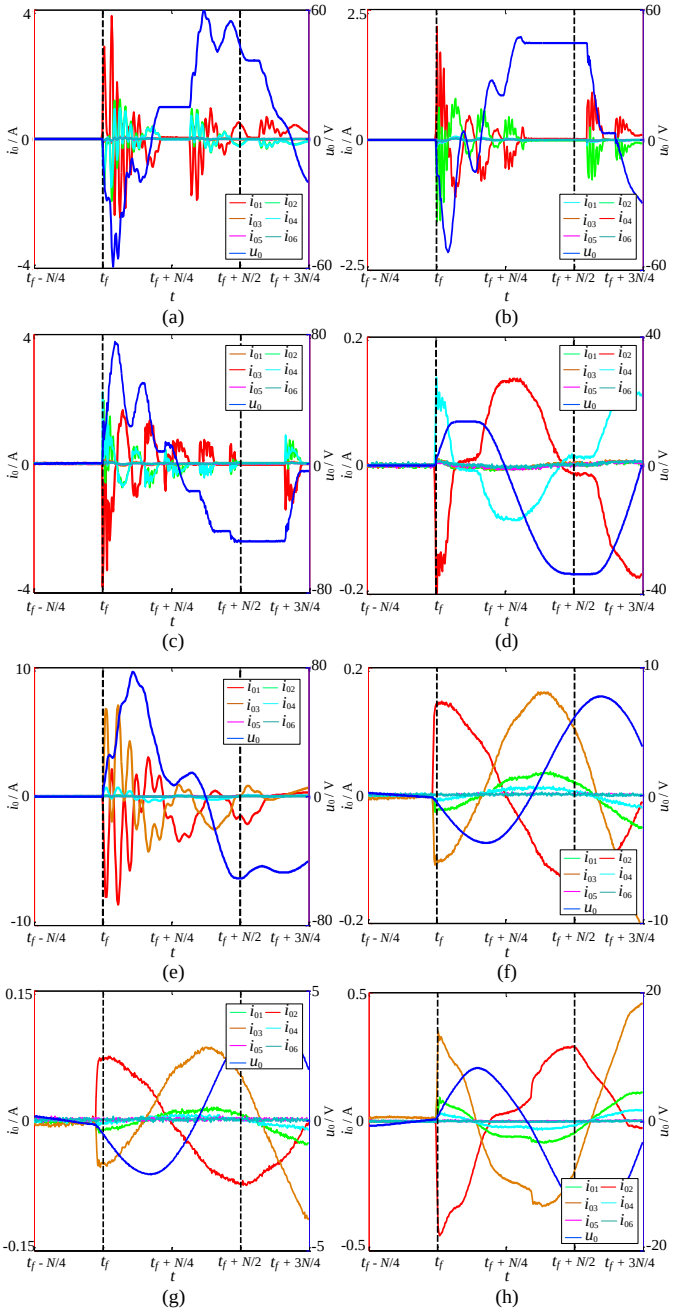

Fig.16. Complete waveforms of ZSV and ZSCs corresponding to Fig. 15.

Typical generated ZSV-ZSC images and the corresponding segmentation results are shown in Fig. 15, and the corresponding complete waveforms are shown in Fig. 16. Evidently, both ZSV and ZSC have huge distortions after the occurrence of SPG faults. In particular, the ZSCs are significantly distorted at the zero-crossing point due to arc extinction and reignition. Despite large distortions in fault signals, the established FCN model with strong learning capability can still conduct waveform segmentation effectively. The calculated fault degree of the faulty feeder is 0.89, 0.98, 0.95, 0.96, 0.96, 0.94, 0.94, and 0.96, respectively, and the fault degree of the healthy feeder are 0.00, 0.00, 0.00, 0.00, 0.00, 0.00, 0.00, and 0.00, respectively. Therefore, the faulty feeder and healthy feeder can be accurately distinguished by using the proposed method.

TABLE XII
DETECTION RESULTS IN FIELD TEST

Detection	S_g	Paper [7]	Paper [39]	Proposed method
Accuracy	Open	100%	44.44%	100%
	Closed	44.44%	44.44%	100%
Average Time	Open	31.11 ms	281.67 ms	26.87 ms
	Closed	31.11 ms	287.78 ms	26.93 ms

Totally 36 sets of fault data were recorded, of which half are obtained from the ungrounded network and half from the resonant grounding network. The detection results are shown in Table XII. Evidently, the huge distortions under arc grounding faults and HIFs would significantly affect the detection performance of the two methods, especially for the paper [39]. In fact, the generalization capability of learning-based methods under new fault scenarios is always the limiting factor for practical applications, and paper [39] fails to accurately detect the faulty feeder when the ZSCs are highly distorted. However, since the proposed method can understand the raw signals on the waveform scale and conduct waveform segmentation effectively, the proposed method can always accurately identify the faulty feeder. Besides, the proposed method also has superior detection efficiency in the embedded device. Therefore, the proposed method exhibits considerable application prospects in practical distribution networks.

E. Fault Data Obtained from Practical Distribution Networks

To verify the detection reliability in practical distribution networks, practical recorded data are used to test the detection performance. Totally 12 sets of fault data are collected from real distribution networks in Chenzhou, Shaoyang, Xiangxi, and Xi'an substation in 2020. Notably, different distribution networks have varied topologies and parameters, where the feeder numbers range from five to eight, and the measurement ratios of CTs in Chenzhou, Shaoyang, Xiangxi, and Xi'an substation are also varied, where they are 100A/1A, 100A/5A, 100A/1A, 150A/5A, respectively. Moreover, the actual fault scenarios contain distinct arcing events of extinction and reignition, especially for SPG faults under the distribution network in Xi'an substation. Typical generated ZSV-ZSC images and the corresponding segmentation results are shown in Fig. 17, and the complete waveforms are depicted in Fig. 18.

It can be clearly seen that there are noticeable distortions in the ZSC waveforms caused by intermittent arc grounding faults, resulting in strong complexity and randomness of fault features. Besides, it may require a rather long time for the arc to reburn when it is extinguished, thereby leading to very long duration for the ZSCs to be zero in waveforms, as shown in Fig. 17 (e) - Fig. 17 (h) and Fig. 18 (e) - Fig. 18 (h). Despite these unfavorable conditions, the established FCN model can still conduct waveform segmentation with high accuracy. It is noteworthy that there are several misclassifications of pixels in Fig. 17 (b) and Fig. 17 (d), where several pixels in Fig. 17 (b) are misclassified as faulty-feeder ZSC and several pixels in Fig. 17 (d) are misclassified as healthy-feeder ZSC. However, the proposed method can evaluate the fault degree on the whole waveform scale, and the estimated fault degree can avoid the influence of misclassifications. Finally, the calculated fault

This article has been accepted for publication in IEEE Transactions on Smart Grid. This is the author's version which has not been fully edited and content may change prior to final publication. Citation information: DOI 10.1109/TSG.2023.3243026

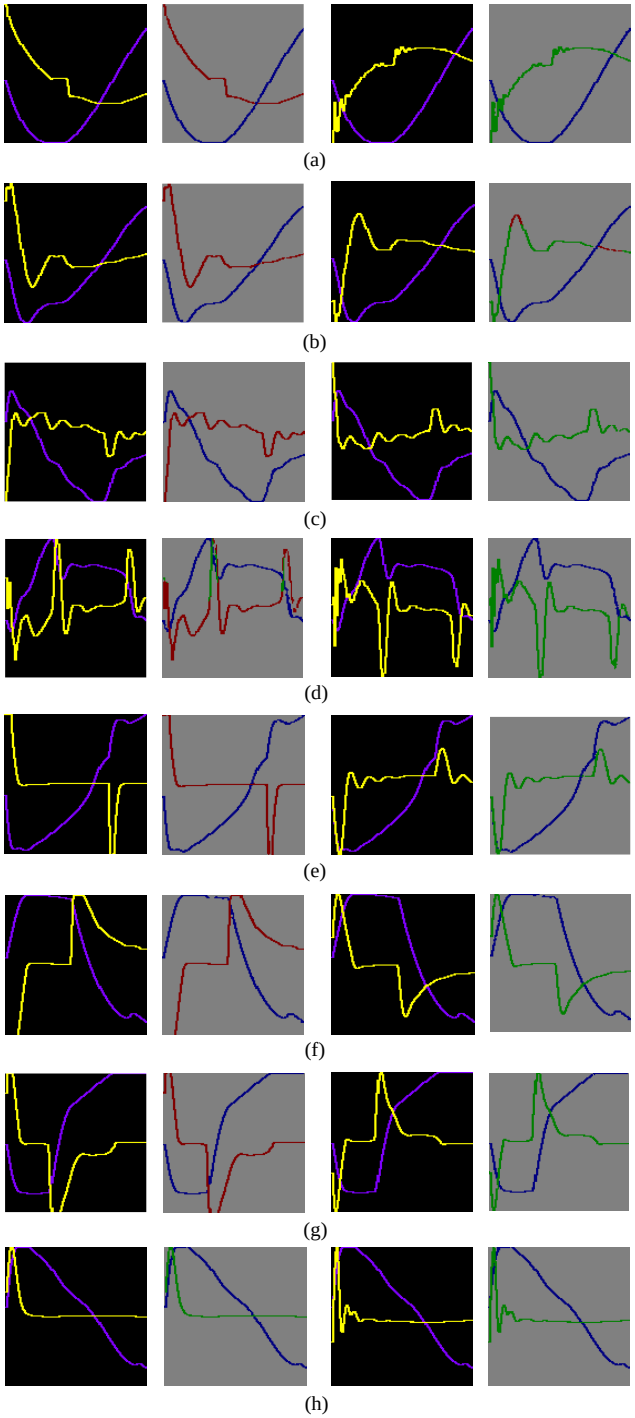

Fig.17. ZSV-ZSC images and the corresponding segmentation results in practical distribution networks (a) fault in feeder 2, Chenzhou substation, the two images correspond to faulty feeder 2 and healthy feeder 3, respectively; (b) fault in feeder 2, Shaoyang substation, the two images correspond to faulty feeder 2 and healthy feeder 4, respectively; (c) fault in feeder 5, Xiangxi substation, the two images correspond to faulty feeder 5 and healthy feeder 2, respectively; (d) fault in feeder 5, Xiangxi substation, the two images correspond to faulty feeder 5 and healthy feeder 4, respectively; (e) fault in feeder 8, Bus I, Xi'an substation, the two images correspond to faulty feeder 8 and healthy feeder 3, respectively; (f) fault in feeder 3, Bus II, Xi'an substation, the two images correspond to faulty feeder 3 and healthy feeder 2, respectively; (g) fault in feeder 3, Bus II, Xi'an substation, the two images correspond to faulty feeder 3 and healthy feeder 6, respectively; (h) fault in Bus I, Xi'an substation, the two images correspond to healthy feeder 4 and 5, respectively.

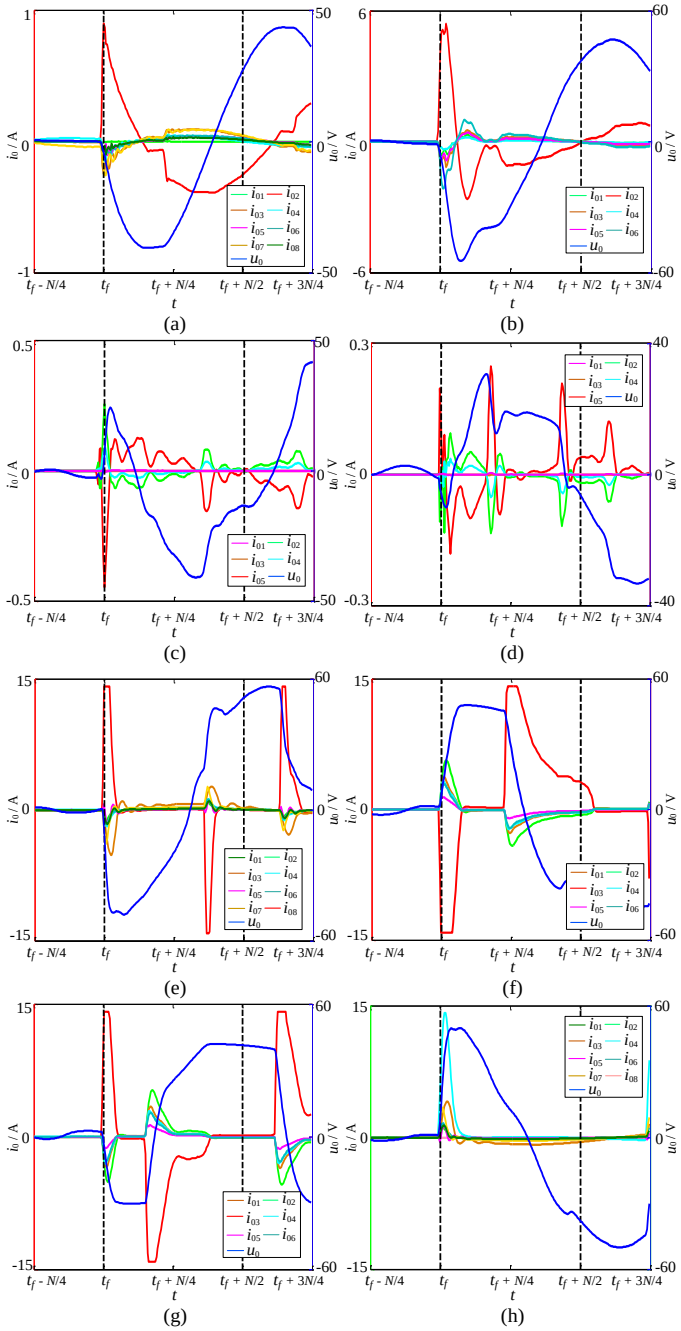

Fig.18. Complete waveforms of ZSV and ZSCs corresponding to Fig. 17.

degree of the faulty feeder in Fig. 17 (a) - Fig. 17 (g) is 0.98, 0.98, 0.99, 0.86, 0.98, 0.99, and 0.99, respectively, while the fault degree of the healthy feeder is 0.00, 0.27, 0.00, 0.00, 0.00, 0.00, and 0.00, respectively, and fault degrees of healthy feeders in Fig. 17 (h) are 0.00 and 0.00. Thus, the proposed method can still work for faulty-feeder detection in practical distribution networks.

The detection accuracy is shown in Table XIII. As shown in Table XIII, both paper [7] and paper [39] have misjudgments for faulty-feeder detection in practical distribution networks. However, the proposed method can still recognize the faulty feeder with 100% detection accuracy and good detection efficiency. Therefore, the proposed method can be implemented in real distribution networks.

TABLE XIII
DETECTION RESULTS IN PRACTICAL DISTRIBUTION NETWORKS

Detection	Paper [7]	Paper [39]	Proposed method
Accuracy	91.67%	75.00%	100%
Average Time	32.04 ms	283.96 ms	27.16 ms

VI. CONCLUSION

To understand raw signals on the waveform scale, this paper proposes a novel faulty-feeder detection method based on the waveform encoding and waveform segmentation. The main conclusions are drawn as follows.

1) Because the waveforms have complete fault features in raw signals, it is necessary to convert the time-series data of ZSV and ZSC into the ZSV-ZSC waveform image. To generate the ZSV-ZSC image quickly, a novel waveform encoding method is proposed, and the image can be obtained within 11 ms in the embedded device, which can guarantee the timely detection of SPG faults.

2) The FCN-based method can learn and recognize the waveforms of ZSV and ZSC by making pixel-wise prediction on the ZSV-ZSC images. After waveform segmentation using the two-path FCN, the segmented waveforms with different categories have clear meanings, and they can be compared with raw waveforms. The credibility of detection results can be evaluated based on fault degree estimation on the similarity between the segmented faulty-feeder ZSC and raw ZSC, thus enhancing the interpretability and reliability of identification.

3) The proposed method is implemented in the NVIDIA Jetson Xavier embedded platform. Besides, both fault data obtained from PSCAD simulation, RTDS HIL test system, field test, and practical distribution networks is utilized to verify the detection performance. The results show that the proposed method not only has over 99.5% detection accuracy under varied fault scenarios, but also can identify the faulty feeder within 28 ms under an SPG fault, thus demonstrating its strong generalization capability and excellent application prospects.

REFERENCES

[1] X. W. Wang, H. X. Zhang, F. Shi, Q. W. Wu, V. Terzija, W. Xie, C. Fang, "Location of Single Phase to Ground Faults in Distribution Networks Based on Synchronous Transients Energy Analysis," *IEEE Trans. Smart Grid*, vol. 11, no. 1, pp. 774–785, Jan, 2020.

[2] C. Lin, W. Gao et al., "Discrete Wavelet Transform-Based Triggering Method for Single-Phase Earth Fault in Power Distribution Systems," *IEEE Trans. Power Del.*, vol. 34, no. 5, pp. 2058-2068, Oct. 2019.

[3] J.W. Yuan, Z. B. Jiao et al., "Study on fault line detection methods based on multi-feature fusion in distribution systems," *IET Gener Transm Distrib*., vol. 15, no. 5, pp. 860–869, Mar. 2021.

[4] J. Gao, X. H. Wang, X. W. Wang, A. J. Yang, H. Yang, X. X. Wei, "A High-Impedance Fault Detection Method for Distribution Systems Based on Empirical Wavelet Transform and Differential Faulty Energy," *IEEE Trans. Smart Grid*, vol. 13, no. 2, pp. 900–912, Mar. 2022.

[5] W. Y. Huang and R. Kaczmarek, " SLG fault detection in presence of strong capacitive currents in compensated networks," *IEEE Trans. Power Del.*, vol. 22, no. 4, pp. 2132–2135, Oct, 2007.

[6] Jin. N, J. W. Xing et al., "A novel Single-phase-to-ground fault identification and isolation strategy in wind farm collector line," *Int. J. Elect. Power Energy Syst.*, vol. 94, pp. 15–26, Jan, 2018.

[7] X. X. Wei, D. C. Yang, X. W. Wang, B. Wang, J. Gao, K. W. Wei, "Faulty feeder detection based on fundamental component shift and multiple-transient-feature fusion in distribution networks," *IEEE Trans. Smart Grid*, vol. 12, no. 2, pp. 1699–1711, March. 2021.

[8] X. W. Wang, X. X. Wei, D. C. Yang, G. B. Song, J. Gao, Y. F. Wei et al., "Fault feeder detection method utilized steady state and transient components based on FFT backstepping in distribution networks," *Int. J. Elect. Power Energy Syst*., vol. 114, Jan. 2020, Art. no. 105391.

[9] Z. Wang and R. S. Balog, "Arc fault and flash signal analysis in DC distribution systems using wavelet transformation," *IEEE Trans. Smart Grid*, vol. 6, no. 4, pp. 1955-1963, Mar. 2015.

[10] A. Borghetti and M. Bosetti, "Integrated use of time-frequency wavelet decompositions for fault location in distribution networks: theory and experimental validation," *IEEE Trans. Power Del*., vol. 25, no. 4, pp. 3139-3146, Oct. 2010.

[11] É. M. Lima and N. Silva, "High impedance fault detection based on stockwell transform and third harmonic current phase angle," *Electric Power Syst. Res*., vol. 175, Oct. 2019, Art. no. 105931

[12] S. Kar and S. R. Samantaray, "Time-frequency transform-based differential scheme for microgrid protection," *IET Gener Transm Distrib*, vol. 8, no. 2, pp. 310–320, Feb. 2014.

[13] X. W. Wang, J. Gao, X. X. Wei, Z. H. Zeng et al., "Single Line to Ground Fault Detection in a Non-Effectively Grounded Distribution Network," *IEEE Trans. Power Del.*, vol. 33, no. 6, pp. 3173−3186, Dec. 2018.

[14] T. Cui, X. Z. Dong et al., "Hilbert-Transform-Based transient/intermittent earth fault detection in noneffectively grounded distribution systems," *IEEE Trans. Power Del.*, vol. 26, no. 1, pp. 143-151, Jan. 2011.

[15] J. W. Yuan, Y. J. Hu, Y. H. Liang, Z. B. Jiao, "Faulty feeder detection for single line-to-ground fault in distribution networks with DGs based on correlation analysis and harmonics energy," *IEEE Trans. Power Del*, early access, 2022, doi: 10.1109/TPWRD.2022.3203992.

[16] X. W. Wang, J. Gao, X. X. Wei, G. B. Song et al., "High impedance fault-detection method based on the variational mode decomposition and Teager–Kaiser energy operators for this distribution network," *IEEE Trans. Smart Grid*, vol. 10, no. 6, pp. 6041–6054, Nov. 2019.

[17] J. W. Yuan, Y. J. Hu, Z. B. Jiao, "Faulty feeder detection method for SLG faults in distribution networks based on comprehensive fault characteristics across entire frequency spectrum," *Int. J. Elect. Power Energy Syst*., vol. 140, Feb. 2022, Art. no. 107835.

[18] Zhai. EJ, Z. Y. Shu, J. Wang et al., "Fault line selection method of small current grounding system based on VMD-LSTM," *Advanced Technology of Electrical Engineering and Energy*, vol 40, no. 1, pp: 70-80, Jan. 2021.

[19] A. Srivastava and S. K. Parida, "A Robust Fault Detection and Location Prediction Module Using Support Vector Machine and Gaussian Process Regression for AC Microgrid," *IEEE Trans. Industry Applications*, vol. 58, no. 1, pp. 930-939, Jan. 2022.

[20] A. Ghaderi, H. A. Mohammadpour, H. L. Ginn and Y. -J. Shin, "High-Impedance Fault Detection in the Distribution Network Using the Time-Frequency-Based Algorithm," *IEEE Trans. Power Del*., vol. 30, no. 3, pp. 1260-1268, June 2015.

[21] S. H. Xiong, Y. D. Liu, J. Fang et al., "Incipient Fault Identification in Power Distribution Systems via Human-Level Concept Learning," *IEEE Trans. Smart Grid*, vol. 11, no. 6, pp. 5239-5248, Nov. 2020.

[22] J. Faiz, S. Lotfi-fard, S. H. Shahri, "Prony-Based Optimal Bayes Fault Classification of Overcurrent Protection," *IEEE Trans. Power Del*., vol. 22, no. 3, pp. 1326-1334, July 2007.

[23] J. J. Q. Yu, Y. H. Hou, A. Y. S. Lam et al., "Intelligent Fault Detection Scheme for Microgrids With Wavelet-Based Deep Neural Networks," *IEEE Trans. Smart Grid*, vol. 10, no. 2, pp. 1694-1703, Mar. 2019.

[24] I. Karmacharya and R. Gokaraju, "Fault Location in Ungrounded Photovoltaic System Using Wavelets and ANN," *IEEE Trans. Power Del*., vol. 33, no. 2, pp. 549-559, April 2018.

[25] Y. Du, Y. D. Liu, Q. Z. Shao, L. G. Luo et al., "Single Line-to-Ground Faulted Line Detection of Distribution Systems with Resonant Grounding Based on Feature Fusion Framework," *IEEE Trans. Power Del*., vol. 34, no. 4, pp. 1766-1775, Aug. 2019.

[26] J. H. Gao, M. F. Guo, D. Y. Chen, "Fault line detection using waveform fusion and one-dimensional convolutional neural network in resonant grounding distribution systems," *CSEE Journal of Power and Energy Systems*, vol. 7, no. 2, pp. 250-260, Mar. 2021.

[27] J. W. Yuan, T. Wu, Y. J. Hu, Z. B. Jiao, "Faulty feeder detection based on image recognition of voltage-current waveforms in non-effectively grounded distribution networks," *Int. J. Elect. Power Energy Syst*., vol. 143, Jun. 2022, Art. no. 108434.

[28] X. Y. Yu, J. Cao, Z. Fan, M. M. Xu and L. Y. Xiao, "Faulty feeder identification in resonant grounding distribution networks based on deep

learning and transfer learning," *CSEE Journal of Power and Energy Systems*, doi: 10.17775/CSEEJPES.2020.05450.

[29] X. W. Wei, X. W. Wang, J. Gao, D. C. Yang, K. W. Wei, L. Guo, "Faulty Feeder Detection for Single-Phase-to-Ground Fault in Distribution Networks Based on Transient Energy and Cosine Similarity," *IEEE Trans. Power Del*., doi: 10.1109/TPWRD.2022.3142186.

[30] J. W. Yuan and Z. B. Jiao, "Faulty feeder detection based on fully convolutional network and fault trust degree estimation in distribution networks," *Int. J. Elect. Power Energy Syst*., vol. 141, Apr. 2022, Art. no. 108264.

[31] J. W. Yuan and Z. B. Jiao, "Faulty feeder detection based on image recognition of current waveform superposition in distribution networks," *Applied Soft Computing*, vol. 130, Nov. 2022, Art. no. 109663.

[32] J. W. Yuan and Z. B. Jiao, "Faulty feeder detection for single phase-to-ground faults in distribution networks based on patch-to-patch CNN and feeder-to-feeder LSTM," *Int. J. Elect. Power Energy Syst*., vol. 147, May. 2023, Art. no. 108909.

[33] J. Long, E. Shelhamer, and T. Darrell, "Fully convolutional networks for semantic segmentation," *Proceedings of the IEEE Conference on Computer Vision and Pattern Recognition (CVPR)*, pp. 3431–3440, 2015.

[34] C. Yu, J. Wang, C. Peng, C. Gao, G. Yu and N. Sang, "Learning a Discriminative Feature Network for Semantic Segmentation," *Proceedings of the IEEE Conference on Computer Vision and Pattern Recognition (CVPR)*, pp. 1857-1866, 2018.

[35] D. R. Lee, "Measures of the Amount of Ecologic Association Between Species," *Ecology*, vol. 26, no. 3, pp. 297-302, Jul. 1945.

[36] K. He, X. Zhang, S. Ren and J. Sun, "Deep Residual Learning for Image Recognition," *2016 IEEE Conference on Computer Vision and Pattern Recognition (CVPR)*, 2016, pp. 770-778.

[37] X. Tang, J. Chen, K. Yang, M. Toyoda, T. Liu, and X. Hu, "Visual Detection and Deep Reinforcement Learning-Based Car Following and Energy Management for Hybrid Electric Vehicles," *IEEE Trans. Trans. Elect*., vol. 8, no. 2, pp. 2501–2515, Jun. 2022.

[38] G. B. Huka, "Modeling and FRT control of grid-connected photovoltaic systems," Ph.D. dissertation, Dept. Elect. Eng. Autom., Harbin Ins. Technol., Harbin, China, 2019.

[39] M. Guo and X. Zeng, "Deep-learning-based earth fault detection using continuous wavelet transform and convolutional neural network in resonant grounding distribution systems," *IEEE Sensors Journal*, vol. 18, no. 3, pp. 1291-1300, Feb. 2018.